Int. J. Electrochem. Sci., 17 **(2022)** Article Number: 220345, doi: 10.20964/2022.03.22

International Journal of
ELECTROCHEMICAL
SCIENCE
www.electrochemsci.org

Preparation and electrochemical properties of silicon embedded in N, P-dual-doped carbon matrix as anode for lithium-ion batteries

Xiaowei Zhou[1], *Yuan Qin*[1], *Yan Dong*[1], *Qing Chang*[2], *Songdong Yuan*[1], *Guodong Jiang*[1,*]

[1] Hubei Collaborative Innovation Center for High-Efficiency Utilization of Solar Energy, School of Materials and Chemical Engineering, Hubei University of Technology, Wuhan 430068, P. R. China
[2] College of Resources and Environmental Science, South-Central University for Nationalities, Wuhan 430074, China
[*]E-mail: jianggd@hbut.edu.cn

Received: 17 November 2021 / *Accepted:* 7 January 2022 / *Published:* 2 February 2022

The disadvantages, such as low electrical conductivity, lithium-ion diffusivity and significant volume expansion of the silicon anode during charge/discharge processes, have severely limited its cycling and rate performance. We proposed a simple method for encapsulating silicon nanoparticles in a nitrogen, phosphorus dual-doped porous carbon matrix, with nitrogen, phosphorus dual-doped carbon derived from phytic acid-doped polyaniline (PANi) hydrogel. Furthermore, the void layer was designed to allow for the volume expansion during silicon lithiation. Scanning electron microscopy and transmission electron microscopy observation indicated that silicon nanoparticles are embedded in the carbon matrix with the presence of a void between the silicon and carbon. The nitrogen adsorption–desorption isotherm showed that the composite featured the hierarchical microporous–mesoporous structure, which was the result of the cross-linking role of phytic acid in PANi; the composites possessed a high specific area of 226.6 m^2/g. The doping level of nitrogen and phosphorus in the composites were 4.7% and 1.2%, respectively. The electrochemical tests indicated that the composite had a much better cyclability with a specific capacity of 639.8 mAh/g after 100 cycles at a current density of 400 mA/g, which was higher than that of silicon encapsulated in a nitrogen-doped carbon. This was attributed to the special porous structure, and the nitrogen, phosphorus dual-doping in carbon materials facilitated the lithiation of silicon anode.

Keywords: silicon, carbon coating, nitrogen, phosphorus, doping

1. INTRODUCTION

Lithium-ion batteries (LIBs) have been widely used in portable equipment, electric vehicles and networked energy storage as efficient energy storage technology because of their high energy density, long cycle life and low cost [1]. Numerous studies have been conducted from the standpoint of electrode

materials to obtain high-performance LIBs with higher energy density, longer cycle life and safety performance [2] to meet the increasing demand. As one of the most promising lithium-ion battery anode materials in the next generation, silicon (Si) has the advantages of high theoretical specific capacity (4200 mAh g^{-1} for $Li_{4.4}Si$ phase), suitable working voltage, earth abundance and environmental friendliness [3]. Moreover, silicon has low conductivity, low lithium-ion diffusivity and a large volume change during the lithiation/delithiation process, which causes electrode pulverisation and gradual loss of electric contact between active materials and current collector [4, 5]. Furthermore, the solid electrolyte interphase (SEI) is repeatedly broken and formed, resulting in repeated consumption of electrolytes [6]. All these issues result in the electrochemical performance degradation of silicon anode.

To date, various strategies have been proposed to surmount these problems. It has been discovered that reducing silicon particles to the nanoscale [7-9] can improve electrochemical performance, which is explained by the reduced stress associated with a large volume effect, a shortened lithium-ion diffusion pathway and increased electrochemical activity. Nonetheless, the tendency of agglomeration and low Coulombic efficiency of nanoscale silicon will inevitably occur due to the larger specific surface area and more SEI formation [10]. Alternatively, the surface coating or modification of silicon by conductive materials, such as graphene [11], carbon nanotubes [12] and conducting polymers [13, 14], are adopted to improve the conductivity and cycling performance. The carbon layer, in particular, not only improves electrical conductivity and protects silicon from electrolyte corrosion but also forms a stable SEI film. Furthermore, carbon coating technology allows for the creation of a wide range of silicon–carbon composite architectures [15-18].

Because heteroatom doping is capable of modulating the electronic properties and electrochemical activity of carbon, non-metal element doping for carbon/silicon composite anodes has attracted considerable attention to promoting electrochemical performance [19-22]. Nitrogen is a particularly interesting doping element; it is shown that nitrogen doping causes defects in carbon, facilitating lithium-ion adsorption and transport. Furthermore, the carbon surface's affinity for the electrolyte will be increased [23]. Due to the occurrence of the synergistic effect, dual-element doping in carbon is regarded as a more promising strategy for promoting the electrochemical performance of carbonaceous materials [24-26]. Owing to the larger radius and smaller electronegativity, replacing the carbon atoms with phosphorus atoms will induce more defects and edge sites. Meanwhile, it can also promote electrochemical performance by enhancing the interaction of Li^+ and accelerating Li^+ diffusion [27]. Recently, Peng et al. [28] developed a composite material composed of nitrogen and phosphorus co-doped carbon-coated silicon oxide. It was demonstrated that the synergistic effect of N, P binary doping increased electronic conductivity and lithium-ion diffusion coefficient to improve electrochemical performance.

Here, we propose a ready method to prepare silicon/carbon composites, in which silicon is embedded in a three-dimensional (3D) hierarchical structural nitrogen, phosphorus dual-doped carbon matrix (denoted as Si@void@NPC). Carbon, nitrogen and phosphorus sources are all simultaneously used in the polyaniline (PANi) hydrogel doped with phytic acid. A silica template layer is also introduced between silicon and carbon to create a void to accommodate volume expansion. Furthermore, the carbonisation of PANi hydrogel encapsulated silicon results in the formation of hierarchical porous

carbon, which effectively accelerates the diffusion of lithium ions. As expected, the Si@void@NPC composites achieve higher reversible capacity, cyclability and rate performance.

2. EXPERIMENTAL SECTION

2.1. Materials synthesis

The Stöber sol–gel method was used to coat commercial silicon nanoparticles (Chaowei Nano, Inc.) with silica. Typically, 0.25 g of Si nanoparticles were dispersed in 75 mL deionised water and 300 mL ethanol and ultrasonicated for 30 min before adding concentrated ammonium hydroxide (5.0 mL, 25%–28%). Under vigorous stirring, 3.6 g tetraethyl orthosilicate (28.4%) was added dropwise, and the reaction was continued for 12 h. The Si@SiO_2 nanoparticles were collected after centrifugation and washed by deionised water and ethanol several times.

PANi hydrogel-coated Si@SiO_2 composite was prepared according to a previously reported method [13, 18, 29]. Si@SiO_2 nanoparticles were dispersed into a mixed solution of 100 mM aniline and 70 mM phytic acid. Following that, a 125 mM ammonium peroxodisulfate solution was added to the above mixture. The mixture gradually became dark green and hydrogel was formed after about 30 min. After freeze-drying, Si@SiO_2@PANi was carbonised at 800 ℃ for 2 h under an Ar atmosphere with a ramping rate of 5 ℃/min to obtain nitrogen and phosphorus dual-doped carbon (Si@SiO_2@NPC). The final Si@void@NPC sample was obtained by immersing Si@SiO_2@NPC in 5% hydrofluoric acid (HF) solution for 50 min to etch the silica layer. Phytic acid was replaced by hydrochloric acid to investigate the former's role in the construction of the nitrogen-doped carbon-encapsulated silicon composites (denoted as Si@void@NC) using the same method as that of Si@void@NPC.

2.2 Structural characterisations

Fourier transform infrared spectroscopy (FT-IR) for the as-prepared samples was carried out on a Thermo Scientific Nicolet iS50 spectrometer. The crystal structure of the sample was analysed using a powder X-ray diffractometer (Empyrean, PANalytical) with a Cu K_α radiation (λ = 1.5406 Å). Scanning electron microscopy (SEM; SU8010, Hitachi) and transmission electron microscopy (TEM; JEM-2100F, JEOL) were used to examine the morphology and microstructure, and an X-ray spectrometer was used for element mapping. The element composition and chemical valence of the samples were examined using a monochromatic X-ray photoelectron spectrometer (K-alpha-F, Thermo Scientific with Al K_α radiation. Nitrogen gas adsorption–desorption isotherms were collected on ASAP 2020 Plus automatic surface area and porosity analyser. The specific surface area and pore size distribution of the samples were determined using the Brunauer–Emmett–Teller (BET) and Barrett–Joyner–Halenda (BJH) methods, respectively.

2.3 Cell fabrication and electrochemical measurements

The working electrode was made by dissolving the active materials, carbon black (Super P) and polyvinylidene difluoride binder in N-methyl pyrrolidone with a mass ratio of 8:1:1 to form a homogeneous slurry. The resulting slurry was then coated on Cu foil using a doctor blade method. After vacuum drying at 80 ℃ overnight, the Cu foil was punched into 12 mm diameter discs with an effective mass loading of 0.3–1 mg/cm^2. The 2032-type half cells, consisting of the active materials as the working electrode, Li foil as the counter and reference electrodes, a Celgard 2300 membrane as the separator and 1 M $LiPF_6$ dissolved in the mixed solvent of ethylene carbonate (EC), dimethyl carbonate (DMC) and diethyl carbonate (DEC) in a volume ratio of 1:1:1 with 10 wt % fluoroethylene carbonate (FEC) as the electrolyte, were assembled in an Ar-filled glove box (H_2O, O_2 < 0.1 ppm). The galvanostatic charge/discharge tests were conducted on the Land CT2001A battery test system in a potential range of 0.01–1.5 V (vs. Li/Li$^+$). Cyclic voltammetry (CV) and electrochemical impedance spectroscopy (EIS) measurements were carried out on Zahner Zennium (Germany) electrochemical workstation. The CV test was completed with a scan rate of 0.1 mV/s between 0.01 and 1.5 V. EIS tests were performed at a frequency range from 10^5 to 0.1 Hz with an amplitude of 5 mV after 100 cycles of charge/discharge. All electrochemical measurements were conducted at about 25℃.

3. RESULTS AND DISCUSSION

Recently, it was reported that the doping ability of phytic acid, as well as the hydrogen bonding and electrostatic interaction between phytic acid and SiO_2 on silicon, allows for the formation of a 3D continuous conductive network hydrogel of silicon/PANi composites [13]. However, because the native silicon dioxide layer on the silicon surface is so thin [30], silicon and phytic acid-doped PANi have a weak interaction. Due to the inferior dispersibility of untreated nano-silicon in an aqueous solution, a layer of silica is coated on the silicon surface through a sol–gel method, which can also improve the interaction between silicon and PANi. The introduced silica can further serve as a void templet, accommodating the volume change of silicon during the charge/discharge cycle. In-situ polymerisation is then used to coat Si@SiO_2 particles with phytic acid-doped PANi hydrogel. PANi conductive hydrogels are typically made by combining two initiators and an aniline-phytic acid [29] solution. Phytic acid-containing six phosphoric acid groups can interact with aniline molecules by protonating the nitrogen groups on the PANi chain, and the protonated imine groups render PANi conductive, which can be used as a dopant and gelator to interact with more than one PANi chain to form a networked hydrogel [13, 29]. When Si@SiO_2 nanoparticles are present in the polymerisation solution, phytic acid is adsorbed on the Si@SiO_2 surface through hydrogen bonding and electrostatic interaction. This will result in the polymerisation of aniline on Si@SiO_2 and further Si@SiO_2 is embedded in the PANi hydrogel network. After carbonisation and etching of the silicon dioxide layer, silicon-based composite is obtained, in which silicon is encapsulated in hierarchical nitrogen, phosphorus co-doped carbon network (denoted as Si@void@NPC) [31, 32].

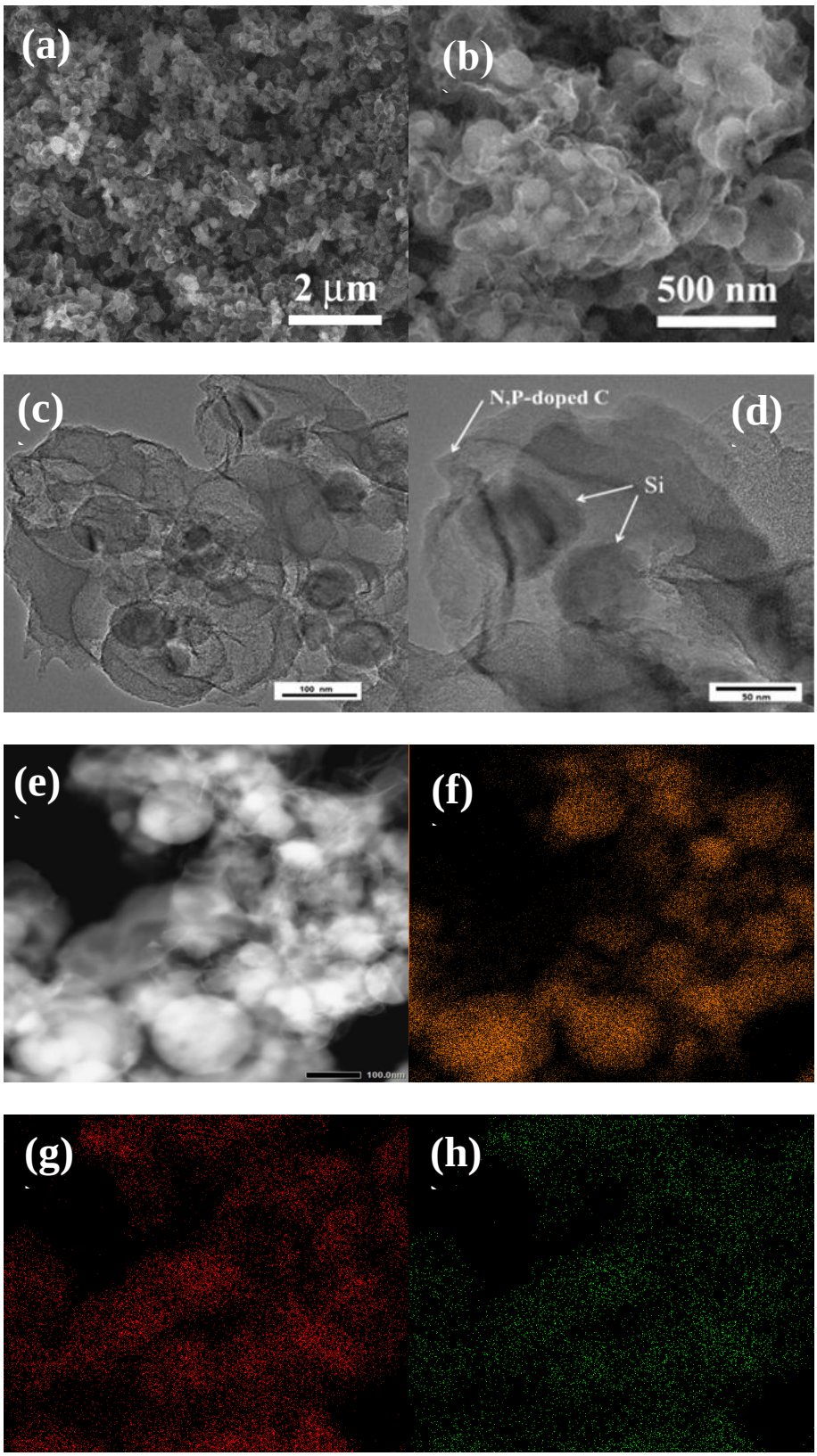
(a)
2 μm
(b)
500 nm
(c)
100 nm
N,P-doped C
Si
(d)
50 nm
(e)
100.0nm
(f)
(g)
(h)

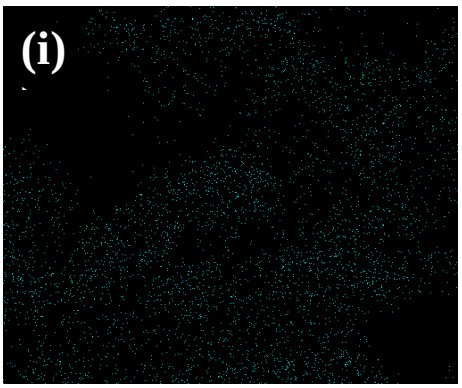

Figure 1. Scanning electron microscopy (a, b) and transmission electron microscopy (TEM) (c, d) images of Si@void@NPC. TEM image (e) of Si@void@NPC and corresponding elemental mapping images of (f) Si, (g) C, (h) N and (i) P.

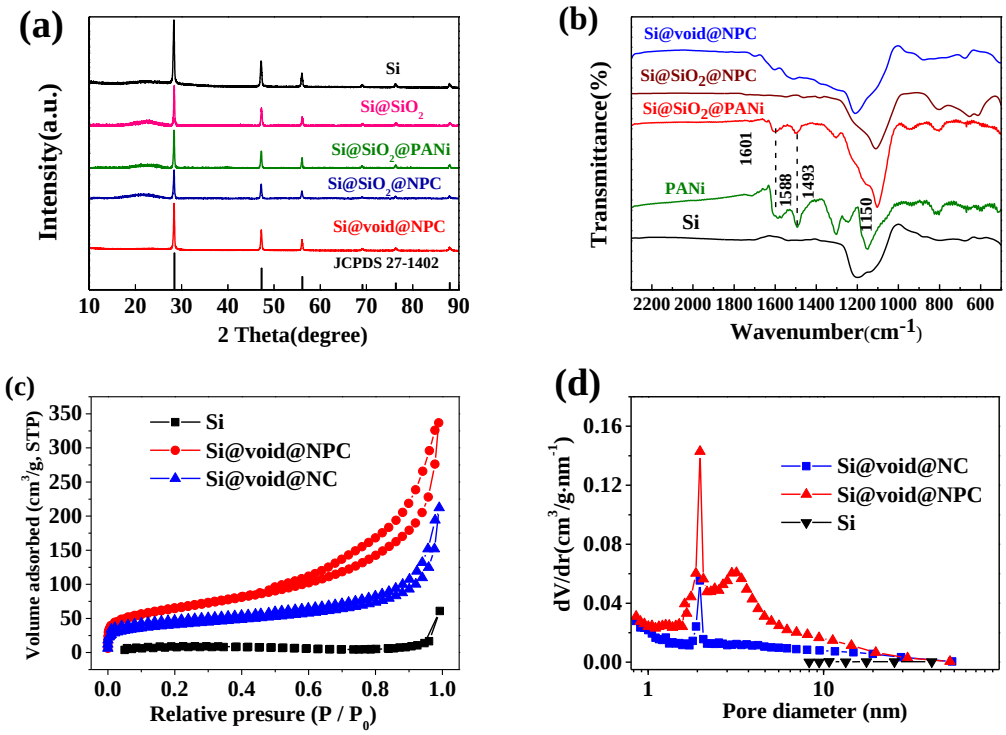

Figure 2. (a) X-ray diffraction patterns of pristine Si and different samples during the preparation of Si@void@NPC composite. (b) Fourier transform infrared spectroscopy spectra of $Si@SiO_2$, PANi, $Si@SiO_2$@PANi, $Si@SiO_2$@NPC and Si@void@NPC composites. (c) N_2 adsorption–desorption isotherms and (d) corresponding pore size distribution of Si, Si@void@NC and Si@void@NPC composites.

The morphology and structure of the Si@void@NPC composite are characterised by SEM and TEM, as shown in Figs. 1(a–d). The carbon derived from PANi hydrogen is observed to be interconnected, forming a 3D architecture. Additionally, silicon nanoparticles have been embedded in a 3D carbon matrix. It is also clear that carbon encapsulation reduces the agglomeration of silicon nanoparticles, which improves silicon nanoparticle stability. The TEM images in Figs. 1(c and d) confirm the presence of void space between the silicon core and carbon, which can accommodate silicon

volume expansion. TEM combined with an energy spectrometer (energy-dispersive X-ray spectroscopy) is used to observe the spatial distribution of different elements in the composites, such as Si, C, N and P. As shown in Fig. 1(f), silicon is uniformly distributed in the spherical shape. Further, carbon is present throughout the spatial area, indicating that silicon nanoparticles are embedded in the interconnected carbon network. The distribution of N and P elements in the composite material is identical to the distribution of carbon elements, indicating that nitrogen and phosphorus have been successfully doped into the carbon matrix and are evenly distributed in the carbon layer.

X-ray diffraction patterns are shown in Fig. 2(a). The pristine silicon, Si@void@NPC has sharp diffraction peaks at 2θ of 28.5°, 47.3°, 56.1°, 69.0°, 76.3° and 88.0°, which can be indexed to the (111), (220), (311), (400), (331) and (422) crystal planes of Si with a cubic structure (JCPDS No. 27-1402), respectively, indicating that high-temperature carbonisation doesn't change the crystal structure. Meanwhile, when coated with silica, a broad weak diffraction peak near 25° appears and then disappears after HF treatment. It will show that a void has formed between the silicon and carbon layers. Carbon diffraction patterns are not observed in the composition, which could be due to carbon's extremely low crystallinity. Additionally, Si@void@NC presents the same diffraction patterns as the Si@void@NPC, showing phytic acid does not alter the crystalline structure of carbon except for providing the phosphorus.

To investigate the structural evolution of the composites during the synthesis of Si@void@NPC composite material, FT-IR spectra of pristine Si, PANi, Si@SiO_2@PANi, Si@SiO_2@NPC and Si@void@NPC are measured, as shown in Fig. 2(b). For PANi, the peaks located at 1588 and 1493 cm^{-1} correspond to the stretching vibration of the quinone and benzene rings, respectively, indicating that PANi is the emeraldine state [29]. The broad absorption peak at 1150 cm^{-1} is also linked to the high electron delocalisation formed by conductive PANi [33]. Si@SiO_2@PANi shows the characteristic peaks of PANi between 1610 and 1100 cm^{-1}, verifying that the Si@SiO_2 particles are successfully composited with PANi. However, the peak for the quinone ring is shifted from 1588 to 1601 cm^{-1}, and the peak for benzene is slightly blue-shifted, implying a possible interaction between PANi and silica [33]. The strong absorption peak at 1103 cm^{-1} is attributed to the antisymmetric stretching of Si–O [34], which overlaps with the peak of PANi at 1150 cm^{-1}. After high-temperature carbonisation, the characteristic peaks of PANi disappear. Through HF treatment, the main peaks for silica disappear, indicating that silica was successfully etched to form the void.

Nitrogen isothermal adsorption/desorption experiments are used to investigate the specific area and porosity of various samples. The results are shown in Figs. 2(c and d). It is discovered that the pristine silicon-adsorbed volume of nitrogen is negligible, and no hysteresis loop exists between the adsorption and desorption branches. For Si@void@NPC, a sharp increase in the low relative pressure range confirms that Si@void@NPC is rich in micropores [35]. Moreover, the isotherm curves display an H4 type hysteresis loop indicative of the presence of mesopores. In the case of Si@void@NC, it has a similar adsorption/desorption behaviour in the low-pressure range but a smaller hysteresis loop. The specific surface area for pristine Si, Si@void@NC and Si@void@NPC composites is calculated to be 29.2, 138.7 and 226.6 m^2/g, respectively, using the BET equation. The special hydrogel structure of PANi mediated by phytic doping may account for the much higher specific area of Si@void@NPC than Si@void@NPC. The BJH model is adopted to calculate the pore size distribution of different materials,

as shown in Fig. 2(d). It reveals that both micropore and mesopore are present and two-pore sizes of 2 and 3.5 nm predominate in Si@void@NPC. Concerning Si@void@NPC, micropores with a size of 2 nm are mainly distributed and few mesopores can be detected. The hierarchical porous structure in the Si@void@NPC composite derived from phytic acid-doped PANi is rationalised by the porous hydrogel structure as well as the evaporation of H_2O, CO_2 and CO during the carbonisation process of PANi [35]. The hierarchical porous carbon layer facilitates the transport and diffusion of electrolytes. Further, it may relieve the compressive stress caused by the volume change during the alloy/de-alloy of silicon, thus improving the mechanical properties of the material.

We used X-ray photoelectron spectroscopy (XPS) to determine the chemical state of nitrogen and phosphorus in the samples; the results are shown in Fig. 3. The survey spectrum in Fig. 3(a) confirms the presence of carbon, nitrogen and phosphorus elements in Si@void@NPC composite, indicating that nitrogen and phosphorus have been successfully incorporated into the carbon material, whereas Si@void@NC contains no phosphorus. Furthermore, the O element is detected in both samples, indicating that it is most likely residual silica or re-oxidised silicon species from the high-temperature carbonisation process.

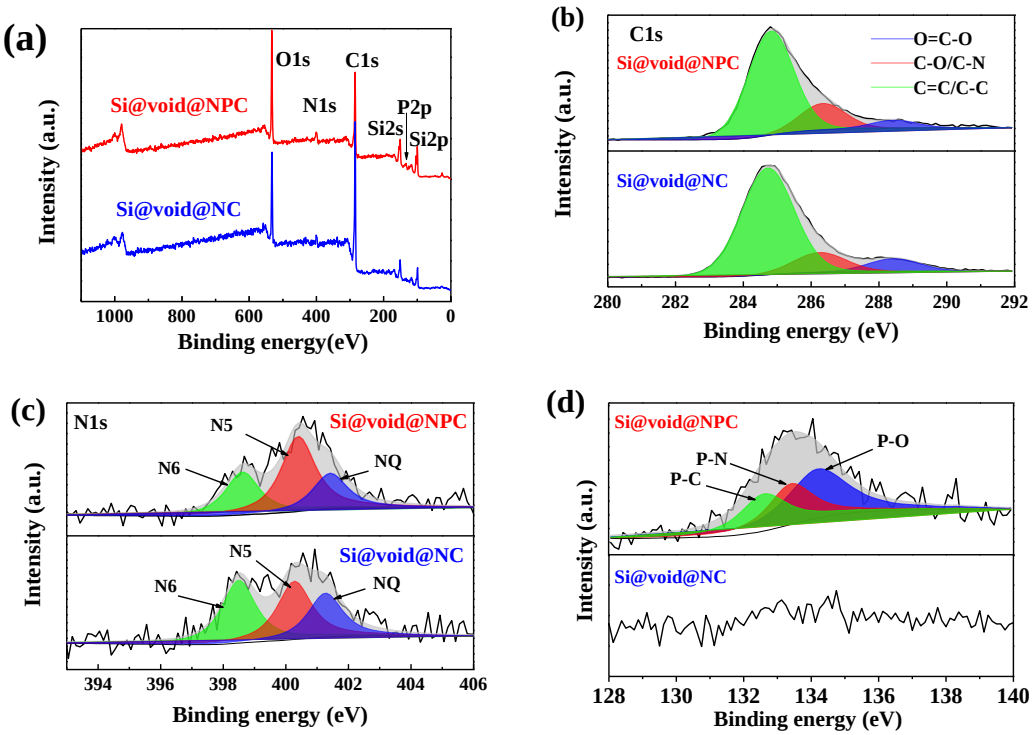

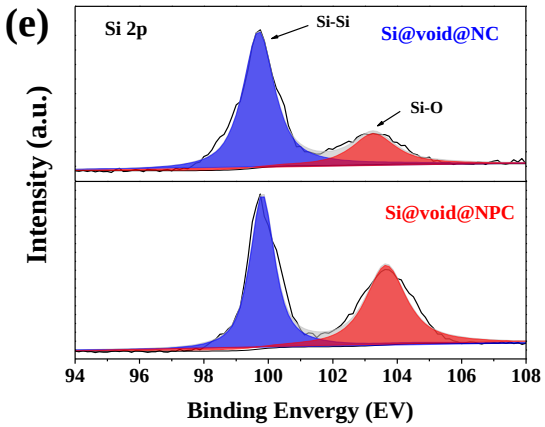

Figure 3. (a) Survey of X-ray photoelectron spectroscopy spectra of the samples and fine spectra of (b) C 1s,(c) N 1s, (d) P 2p and (e) Si 2p of Si@void@NC and Si@void@NPC composites.

The nitrogen atomic content in Si@void@NPC is calculated to be 4.7%, which is higher than that of 3.4% in Si@void@NC. Meanwhile, the phosphorus content in Si@void@NPC is measured to be 1.2%. The doping level of phosphorus in Si@void@NPC is relatively low, which is attributed to the fact of the small molecule phytic acid interacting with PANi through electrostatic interaction and hydrogen bonding partially converting to gas and escaping during the high-temperature process. The C 1s spectra for both samples are shown in Fig. 3(b). The peaks located at 284.8, 286.3 and 288.5 eV are assigned to C–C/C=C, C–O/C–N and O=C–O groups, respectively. [20] The high-resolution N 1s spectrum consists of three peaks centred at 398.5, 400.2 and 401.3 eV, which are attributed to pyridinic N (N6), pyrrolic N (N5) and graphitic N (NQ), respectively [23]. Figure 3(d) shows the fine spectrum of P 2p in the Si@void@NPC composite. It is deconvoluted to three peaks at 132.7, 133.5 and 134.3 eV, which correspond to the bonds of P–C, P–N and P–O, respectively [36]. The high-resolution XPS spectra of Si 2p in Fig. 3(e) display two main peaks centred at 99.9 and 103.6 eV, corresponding to Si−Si and Si−O bonds, respectively [16].

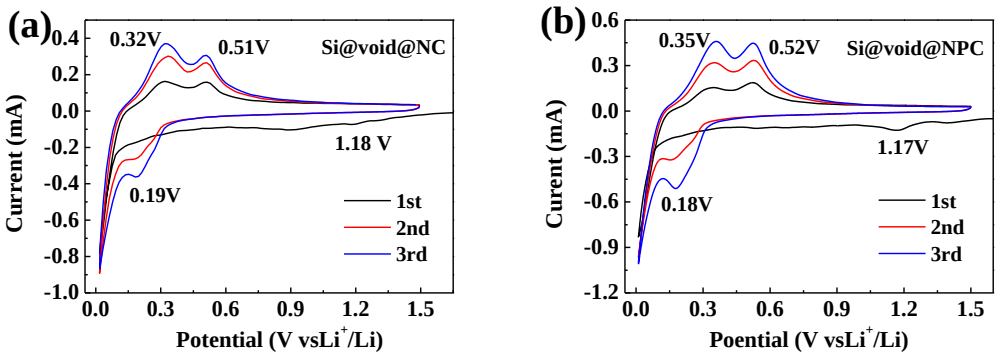

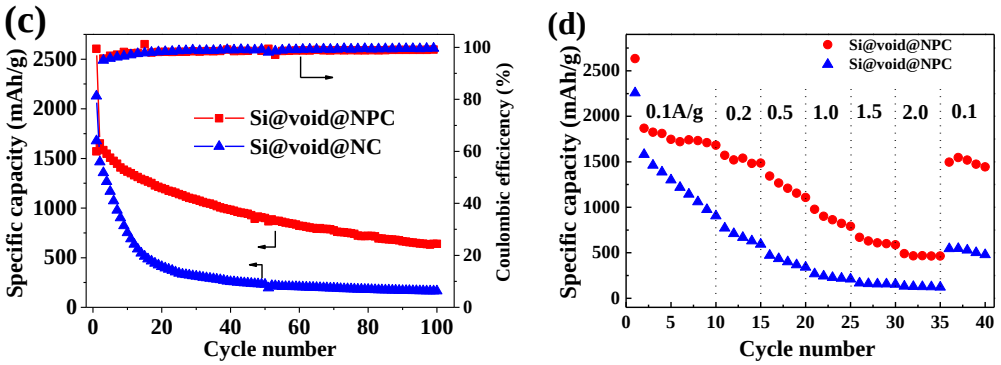

Figure 4. Cyclic voltammetry curves for the first three cycles of (a) Si@void@NC and (b) Si@void@NPC. (c) Cyclic performance at a current density of 0.4 A/g and (d) rate performance of Si@void@NPC and Si@void@NC composites.

The lithiation/delithiation behaviour of Si@void@NC and Si@void@NPC composites is investigated using CV, as demonstrated in Figs. 4(a and b). The two composites have the typical electrochemical properties of Si-based materials at a sweep rate of 0.1 mV/s. Further, a weak cathodic peak at 1.18 V in the first cycle corresponds to the reduction process of FEC for Si@void@NC. Meanwhile, several peaks arising from the reduction of the mixed solvent of EC, DMC and DEC in the range of 0.6–0.9 V are also visible. [37, 38] All the electrolyte reduction will contribute to the formation of a stable SEI film on the surface of the composite. The reduction peak near 0.18 V is related to the alloying of silicon and formation of irreversible Li_2O and Li_xSiO_y. During the delithiation process, two oxidation peaks centred at 0.35 and 0.52 V are associated with the dealloying process of Li_xSi to form amorphous Si [39]. In the following scans, the intensity of the redox peaks gradually increases, which is due to the gradual activation process of silicon during the alloy/dealloying process [40], while the peak position remains unchanged, indicating that Si@void@NC forms a stable interface layer. The reduction of FEC additive and mixed solvent is nearly identical to that of Si@void@NPC for Si@void@NPC composite, except for the minor differences in the peak strength and position, which may result from co-doping of nitrogen and phosphorus in carbon coating.

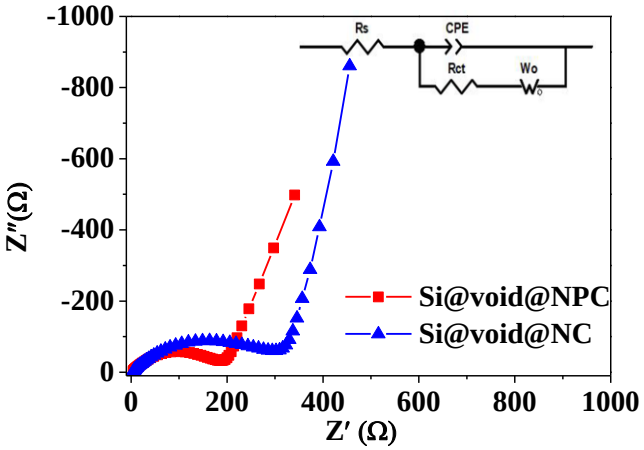

Figure 5. Nyquist of Si@void@NPC and Si@void@NC composite electrodes.

Galvanostatic charge–discharge and rate performance tests are performed on Si@void@NC and Si@void@NPC composites and the results are displayed in Figs. 4(c and d). In contrast to Si@void@NC delivering an initial discharge capacity of 2127 mAh/g in the first cycle, Si@void@NPC shows a higher discharge capacity of 2604 mAh/g, which is probably ascribed to its higher specific area and nitrogen, phosphorus co-doping. The capacity drastically decreases to 1650 mAh/g in the second cycle and decays much slower in the following cycle. The Coulombic efficiency of Si@void@NPC for the first cycle is 60.0%, which is slightly lower than the Coulombic efficiency of Si@void@NC of 64.41%. It can be explained by the formation of SEI film with a larger specific surface area and an increase of dangling bonds in the carbon layer caused by nitrogen, phosphorus co-doping, resulting in irreversible capacity loss. Nevertheless, the Coulombic efficiency of Si@void@NPC quickly increases to 93% in the second cycle and reaches over 98% in the tenth cycle. From Fig. 4(c), it is discovered that Si@void@NC has poor cycle stability. The specific capacity of Si@void@NC rapidly decays after several cycles, and it only delivers a discharge specific capacity of 163.9 mAh/g after 100 cycles. Si@void@NPC electrode maintains a relatively stable cycle performance. The discharge-specific capacity remains 639.8 mAh/g after 100 cycles at a current density of 0.4 A/g. Furthermore, the rate performance is further investigated at varied current densities. Si@void@NPC shows discharge-specific capacities of 1631, 1454.4, 1093, 783.4, 582.3 and 459.4 mAh/g at current densities of 0.1, 0.2, 0.5, 1, 1.5 and 2 A/g, respectively, as displayed in Fig. 4(d). It is visible that in contrast to Si@void@NC, Si@void@NPC shows a better rate performance. When the current density is reduced to 0.1 A/g, its reversible specific capacity nearly recovers to the original level of 1403.6 mAh/g, demonstrating that the Si@void@NPC composite material has better structural stability.

Table 1. The comparison of the result in this work with other works' results.

Materials	Potential range(V vs Li^+/Li)	Current density(A/g)	Discharge specific capacity(mAh/g)
Si@void@NPC	0.01–1.5	0.4	639.8 (after 100 cycles)
SHCM/NCF[42]	0.0–3.0	0.5	450 (after 200 cycles)
N-doped orderedmesoporous carbon/silica(N-OMC/SiO_2)[43]	0.01–3	0.1	740 (after 50 cycles)
3D Si/NGC[44]	0.01–1.5	0.2	900 (after 300 cycles)
the core-shell Si/nitrogen-doped carbon (Si/N-C)[45]	0.01–2.0	0.2	1084 (after 50 cycles)
Si-rGO/NCT composite[46]	0.01–1.2	0.1	892.3 (after 100 cycles)
2D NPC/C@Si[47]	0.01–2	0.2	592 (after 100 cycles)

The improved electrochemical performance of the Si@void@NPC composite is attributed to the co-doping of nitrogen and phosphorus, which causes more defects and edge sites in the carbon layer, resulting in a discharge-specific capacity. Simultaneously, the cross-linking effect of phytic acid during the polymerisation process also increases the specific area, and improves the structural stability of the

composite, contributing to the higher cycle stability. Compared to other silicon–carbon cathode materials, Si@void @NPC composites show excellent electrochemical properties. Table 1 shows the discharge specific capacity of various silicon–carbon-negative materials at different current densities. We can see from the comparison that nitrogen doping or nitrogen and phosphorus double doping can maintain good electrochemical performance over a long cycle.The EIS tests are conducted to investigate lithiation/delithiation kinetics of the active materials after the cycling, as displayed in Fig. 5. It is noticeable that the Nyquist plots for Si@void@NPC and Si@void@NC composites consist of a semicircle and a declined line, which correspond to the charge transfer resistance (R_{ct}) between the electrode/electrolyte interface and diffusion impedance (W) of lithium-ion inside the battery [41], respectively. When fitted with the equivalent circuit, the R_{ct} of Si@void@NC and Si@void@NPC composites are 314 and 192 Ω, respectively. The electrochemical activity Si@void@NPC electrode is sequentially increased corresponding to the decrease in R_{ct}. It is has been reported that N, P-dual-doping will effectively increase the electrical conductivity of the carbon layer [28], which could explain why N, P-dual-doping improves the activity of Si anodes.

4. CONCLUSION

In conclusion, we have proposed a simple method for a Si-based anode. The PANi gel doped with phytic acid was simultaneously used as carbon, nitrogen and phosphorus sources and further composited with silica-coated silicon nanoparticles. After pyrolysis and selective etching, silicon encapsulated in nitrogen-phosphorus co-doped carbon with a 3D interconnected network was obtained. Additionally, the void between the silicon core and carbon layer is created to accommodate the volume change of silicon during the lithium alloying/dealloying process. The 3D porous hierarchical carbon framework accelerated the infiltration of electrolytes, thereby promoting the transport of ions. Nitrogen, phosphorus dual-doping in the carbon framework reduced the interfacial charge transfer impedance, resulting in higher cyclability and rate performance of the silicon-based anodes.

ACKNOWLEDGMENTS
This work was supported by grants from Hubei Province Technology Innovation Project (2018AAA056) and the opening fund of Key Laboratory of Material Chemistry for Energy Conversion and Storage (HUST), Ministry of Education.

References

1. Y. Liu, Y. Zhu and Y. Cui, *Nature Energy*, 4 (2019) 540.
2. M. Ashuri, Q. He and L.L. Shaw, *Nanoscale,* 8 (2016) 74.
3. M.A. Rahman, G. Song, A.I. Bhatt, Y.C. Wong and C. Wen, *Adv. Funct. Mater.,* 26 (2016) 647.
4. F.M. Hassan, A.R. Elsayed, V. Chabot, R. Batmaz, X. Xiao and Z. Chen, *ACS Appl. Mater. Interfaces,* 6 (2014) 13757.
5. H. Kim, M. Seo, M.-H. Park and J. Cho, *Angew. Chem. Int. Ed*., 49 (2010) 2146.
6. E. Pollak, G. Salitra, V. Baranchugov and D. Aurbach, *J. Phys. Chem*. C, 111 (2007) 11437.

7. M.T. McDowell, I. Ryu, S.W. Lee, C. Wang, W.D. Nix and Y. Cui, *Adv. Mater*., 24 (2012) 8.
8. M.-H. Park, M.G. Kim, J. Joo, K. Kim, J. Kim, S. Ahn, Y. Cui and J. Cho, *Nano Lett*., 9 (2009) 3844.
9. M.R. Zamfir, N. Hung Tran, E. Moyen, Y.H. Lee and D. Pribat, *J. Mater. Chem.* A ,1 (2013) 9566.
10. M. Wu, J.E.C. Sabisch, X. Song, A.M. Minor, V.S. Battaglia and G. Liu, *Nano Lett*., 13 (2013) 5397.
11. Y. Zhu, W. Liu, X. Zhang, J. He, J. Chen, Y. Wang and T. Cao, *Langmuir,* 29 (2013) 744.
12. X. Zhou, Y. Liu, C. Du, Y. Ren, T. Mu, P. Zuo, G. Yin, Y. Ma, X. Cheng and Y. Gao, *J. Power Sources,* 381 (2018) 156.
13. H. Wu, G. Yu, L. Pan, N. Liu, M.T. McDowell, Z. Bao and Y. Cui, *Nat. Commun*., 4 (2013) 1943.
14. W. Shi, H.B. Wu, J. Baucom, X. Li, S. Ma, G. Chen and Y. Lu, *ACS Appl. Mater. Interfaces,* 12 (2020) 39127.
15. S. Zhao, C. Yao, L. Sun and X. Xian, *Ionics,* 24 (2018) 1039.
16. S. Guo, X. Hu, Y. Hou and Z. Wen, *ACS Appl. Mater. Interfaces,* 9 (2017) 42084.
17. N. Liu, Z. Lu, J. Zhao, M.T. McDowell, H.-W. Lee, W. Zhao and Y. Cui, *Nat. Nanotechnol*., 9 (2014) 187.
18. H.S. Oh, H.M. Jeong, J.H. Park, I.-W. Ock and J.K. Kang, *J. Mater. Chem*. A, 3 (2015) 10238.
19. R. Xu, G. Wang, T. Zhou, Q. Zhang, H.-P. Cong, S. Xin, J. Rao, C. Zhang, Y. Liu, Z. Guo and S.-H. Yu, *Nano Energy,* 39 (2017) 253.
20. C. Zhang, X. Cai, W. Chen, S. Yang, D. Xu, Y. Fang and X. Yu, *ACS Sustain. Chem. Eng*., 6 (2018) 9930.
21. S. Huang, L.-Z. Cheong, D. Wang and C. Shen, *ACS Appl. Mater. Interfaces,* 9 (2017) 23672.
22. F. Li, M. Zhu, Z. Luo, L. Guo, Z. Bian, Y. Li and K. Luo, *J Solid State Electrochem.,* 23 (2019) 2391.
23. Y. Xie, Y. Chen, L. Liu, P. Tao, M. Fan, N. Xu, X. Shen and C. Yan, *Adv. Mater*. 29 (2017) 1702268.
24. X. Zhou, J. Tian, Q. Wu, J. Hu and C. Li, *Energy Storage Mater.,* 24 (2020) 644.
25. H. Shan, X. Li, Y. Cui, D. Xiong, B. Yan, D. Li, A. Lushington and X. Sun, *Electrochim. Acta,* 205 (2016) 188.
26. Q. Pang, J. Tang, H. Huang, X. Liang, C. Hart, K.C. Tam and L.F. Nazar, *Adv. Mater*., 27 (2015) 6021.
27. X. Zhang, Z. Lu, Z. Fu, Y. Tang, D. Ma and Z. Yang, *J. Power Sources,* 276 (2015) 222.
28. M. Peng, Y. Qiu, M. Zhang, Y. Xu, L. Yi and K. Liang, *Appl. Surf. Sci*., 507 (2020) 145060.
29. L. Pan, G. Yu, D. Zhai, H.R. Lee, W. Zhao, N. Liu, H. Wang, B.C.K. Tee, Y. Shi, Y. Cui and Z. Bao, *Proc. Natl. Acad. Sci*., 109 (2012) 9287.
30. A. Athanassouli, T. Ganetsos, F. Klose and S. Messoloras, *Semicond. Sci. Technol*., 17 (2001) 65.
31. G. Mu, Z. Ding, D. Mu, B. Wu, J. Bi, L. Zhang, H. Yang, H. Wu and F. Wu, *Electrochim. Acta,* 300 (2019) 341.
32. J. Zhang, Y. Shi, Y. Ding, L. Peng, W. Zhang and G. Yu, *Adv. Energy Mater*., 7 (2017) 1602876.
33. P.N. Moghadam, J. Khalafy and T. Taheri, *Polym. Adv. Technol*., 21 (2010) 235.
34. H. Wei, H. Gu, J. Guo, S. Wei, J. Liu and Z. Guo, *J. Phys. Chem*. C, 117 (2013) 13000.
35. G. Xu, B. Ding, J. Pan, J. Han, P. Nie, Y. Zhu, Q. Sheng and H. Dou, *J. Mater. Chem*. A, 3 (2015) 23268.
36. H. He, D. Huang, Y. Tang, Q. Wang, X. Ji, H. Wang and Z. Guo, *Nano Energy,* 57 (2019) 728.
37. Y. Jin, N.-J.H. Kneusels, P.C.M.M. Magusin, G. Kim, E. Castillo-Martinez, L.E. Marbella, R.N. Kerber, D.J. Howe, S. Paul, T. Liu and C.P. Grey, *J. Am. Chem. Soc*., 139 (2017) 14992.
38. T. Mu, P. Zuo, S. Lou, Q. Pan, Q. Li, C. Du, Y. Gao, X. Cheng, Y. Ma and G. Yin, *Chem. Eng. J*., 341 (2018) 37.
39. Q. Pan, P. Zuo, T. Mu, C. Du, X. Cheng, Y. Ma, Y. Gao and G. Yin, *J. Power Sources,* 347 (2017) 170.

40. C. Li, C. Liu, K. Ahmed, Z. Mutlu, Y. Yan, I. Lee, M. Ozkan and C.S. Ozkan, *RSC Adv*., 7 (2017) 36541.
41. Y. Bie, J. Yang, W. Lu, Z. Lei, Y. Nuli and J. Wang, *Electrochim. Acta,* 212 (2016) 141.
42. Y.R. Liang, L.F. Cai, L.Y. Chen, X.D. Lin, R.W. Fu, M.Q. Zhang, D.C. Wu, Nanoscale, 7 (2015) 3971.
43. Y.R. Liang, L.F. Cai, L.Y. Chen, X.D. Lin, R.W. Fu, M.Q. Zhang, D.C. Wu, *Nanoscale*, 7 (2015) 3971.
44. T.S. Mu, P.J. Zuo, S.F. Lou, Q.R. Pan, H. Zhang, C.Y. Du, Y.Z. Gao, X.Q. Cheng, Y.L. Ma, H. Huo, *J. Alloys Compd.*, 777 (2019) 190
45. L.X. Zeng, R.P. Liu, H.Y. Qiu, X. Chen, X.X. Huang, P.X. Xiong, Q.R. Qian, Q.H. Chen, M.D. Wei, *Funct. Mater. Lett.*, 9 (2016) 1650055
46. X.F. Tang, G.W. Wen, Y. Zhang, D. Wang, Y. Song, *Appl. Surf. Sci.*, 425 (2017) 742
47. C.Z. Ke, F. Liu, Z.M. Zheng, H.H. Zhang, M.T. Cai, M. Li, Q.Z. Yan, H.X. Chen, Q.B. Zhang, *Rare Met.*, 40 (2021) 1347